Micro and Nanostructures 218 (2026) 208836

Contents lists available at ScienceDirect

Micro and Nanostructures

journal homepage: www.journals.elsevier.com/micro-and-nanostructures

Influence of external electric field on the shallow donor impurity states in a double parabolic quantum dot

E. Kasapoglu [a], Melike Behiye Yücel [b], C.A. Duque [c,*]

[a] Sivas Cumhuriyet University, Faculty of Science, Physics Department, 58140 Sivas, Türkiye
[b] Department of Physics, Science Faculty, Akdeniz University, 07058 Antalya, Türkiye
[c] Grupo de Materia Condensada-UdeA, Instituto de Física, Facultad de Ciencias Exactas y Naturales, Universidad de Antioquia UdeA, Calle 70 No. 52-21, Medellín, Colombia

ARTICLE INFO

Keywords:
Double parabolic quantum dot
Donor impurity
Electric field

ABSTRACT

We present a theoretical investigation of the confined electronic states in a two-dimensional double parabolic quantum dot subjected to external electric fields and Coulomb impurities within the effective-mass approximation. The electronic spectrum is analyzed as a function of the confinement geometry, impurity configuration, electric-field magnitude, and field orientation. The confinement potential enables a continuous transition from a strongly coupled double-quantum-dot regime with pronounced central barriers and localization effects to a single-dot-like flat-bottom confinement profile.

The results reveal that the interplay between confinement topology, impurity-induced asymmetry, and external electric fields strongly modifies the confined energy spectrum. In asymmetric impurity configurations, the breaking of inversion symmetry induces pronounced linear contributions to the quantum-confined Stark effect, whereas symmetric Coulomb configurations restore predominantly quadratic Stark behavior governed by the polarizability of the confined states. The calculations further show the emergence of field-induced anticrossings, electric-field-controlled hybridization between low-lying states, and angular modulation of the electronic energies associated with the vectorial nature of the applied field.

The study also demonstrates that the geometrical parameters controlling the central barrier and the flat-bottom confinement significantly influence localization properties, tunneling coupling, and the compression of excited-state spectra at high electric fields. These results provide a detailed understanding of the combined role of geometry, impurity distribution, and external perturbations in tailoring the electronic structure of low-dimensional semiconductor nanostructures and establish a theoretical framework that may be useful for future investigations of field-controlled quantum devices and related optical phenomena.

1. Introduction

Quantum confinement in semiconductor nanostructures has been extensively investigated due to both its fundamental physical interest and technological potential. By controlling geometry, composition, and external perturbations, quantum-confined systems exhibit highly tunable electronic properties that are inaccessible in bulk materials. As a consequence, quantum dots (QDs) have become relevant building blocks for applications in sensing, optoelectronics, energy technologies, biomedicine, photovoltaics, and quantum devices [1–7].

* Corresponding author.
E-mail address: carlos.duque1@udea.edu.co (C.A. Duque).

https://doi.org/10.1016/j.micrna.2026.208836
Received 8 April 2026; Received in revised form 9 June 2026; Accepted 10 July 2026
Available online 16 July 2026
2773-0123/© 2026 Elsevier Ltd. All rights are reserved, including those for text and data mining, AI training, and similar technologies.

Early studies focused mainly on III–V semiconductor QDs, where many-body interactions, Coulomb blockade, and tunneling phenomena were widely explored [8,9]. External electric fields were shown to induce Stark shifts and symmetry breaking in confined states [10–12], while donor impurities and Coulomb centers were found to strongly modify localization and electronic spectra [13–16]. The extension from single QDs to coupled double quantum dots (DQDs) introduced molecular-like bonding and antibonding states, making these systems particularly attractive for quantum information processing and artificial-molecule implementations [17,18]. Due to the presence of tunnel-coupled confinement regions, DQDs are especially sensitive to external perturbations and impurity-induced asymmetries.

The emergence of two-dimensional materials further expanded the scope of quantum confinement research. In these systems, reduced dielectric screening and enhanced Coulomb interactions enabled the realization of gate-defined QDs and DQDs with strong tunability [19–21]. Within this context, two-dimensional effective-mass models provide a suitable framework for describing the interplay between confinement, Coulomb interactions, and externally applied fields.

Field-induced control of carrier localization, tunneling rates, and level hybridization has been shown to play a central role in determining the electronic structure and quantum-confined Stark effect in coupled quantum-dot systems [22–26]. Since these electronic properties constitute the basis of many optical and transport phenomena, understanding their behavior under external perturbations remains of considerable theoretical and technological interest [27–30].

Coupled QD systems have also attracted attention in the context of resonant transport and coherence phenomena [31–33]. From a theoretical perspective, these effects are highly sensitive to the accurate determination of confined energy levels and wave functions under external perturbations.

Despite the considerable progress achieved in the study of coupled QDs, the combined influence of external electric fields, impurity-induced asymmetry, and geometrically controlled double-well confinement on the confined electronic spectrum remains insufficiently understood. In particular, the interplay between field-driven localization, Coulomb-induced symmetry breaking, anticrossing formation, and angular Stark modulation has not yet been systematically analyzed within a unified two-dimensional effective-mass framework. Addressing these aspects is essential for understanding how external perturbations can be used to engineer the electronic properties of coupled semiconductor nanostructures.

In this context, a detailed understanding of the confined electronic spectrum constitutes a fundamental step toward describing more complex physical phenomena in coupled nanostructures. In particular, the interplay between confinement topology, impurity-induced asymmetry, and externally applied electric fields can strongly modify localization properties, tunnel coupling, level hybridization, and Stark shifts, thereby providing multiple mechanisms for tailoring the electronic behavior of low-dimensional systems.

Motivated by these considerations, the present work develops a two-dimensional effective-mass model for a double parabolic quantum dot subjected simultaneously to external electric fields and Coulomb impurities. The study focuses on the evolution of the confined electronic states as functions of the confinement geometry, impurity configuration, electric-field magnitude, and field orientation. Particular attention is devoted to the emergence of impurity-induced asymmetry, field-controlled localization, anticrossings, and the transition between double-dot and flat-bottom confinement regimes. The results provide a systematic analysis of the quantum-confined Stark effect and the mechanisms governing the tunability of confined electronic states in coupled semiconductor nanostructures.

The remainder of this article is organized as follows. Section 2 presents the theoretical framework and numerical approach. Section 3 discusses the effects of electric fields, impurity position, and geometrical parameters on the confined electronic spectrum. Finally, the main conclusions are summarized in Section 4.

2. Theoretical framework

We consider a single charge carrier confined in a 2D DQD structure, described within the effective-mass approximation. The system is modeled by a lateral confinement potential that defines two coupled QDs separated by a finite tunneling barrier and is subjected to a uniform in-plane external electric field. In addition, a Coulomb impurity is introduced as a localized charge center, whose position relative to the confinement geometry can be varied to accommodate different impurity configurations. Within this framework, the carrier dynamics are governed by a 2D Schrödinger equation that explicitly includes the confinement potential, the electric-field interaction term, and the Coulomb impurity potential. This formulation provides a consistent basis for analyzing the interplay between confinement geometry, impurity-induced asymmetry, and field-driven localization effects on the confined energy spectrum and wave functions.

2.1. Effective-mass Schrödinger equation

Within the single-band effective mass approximation, the electron envelope function $\psi(x,y)$ satisfies the two-dimensional Schrödinger equation

$$\left[-\frac{\hbar^2}{2m^*}\left(\frac{\partial^2}{\partial x^2}+\frac{\partial^2}{\partial y^2}\right)+V(x,y)+V_{\mathrm{C}}(x,y)+V_{\mathrm{F}}(x,y)\right]\psi(x,y)=E\,\psi(x,y), \tag{1}$$

where m^* is the effective electron mass (in this work, $m^*=0.067\,m_0$, corresponding to the effective GaAs electron mass, with m_0 being the free electron mass), $\hbar$ is the reduced Planck constant, and E denotes the confined energy eigenvalues.

2.2. Confinement potential

The lateral confinement is modeled by a double parabolic potential modulated by a Gaussian term, defined as

$$g(x,y) = V_0 \left[\frac{x^2+y^2}{R_1^2} + \exp\left(-\frac{x^2}{R_2^2} \right) \right], \tag{2}$$

where R_1 sets the global parabolic confinement length scale, R_2 controls the width of the Gaussian modulation, and $V_0 = \beta V_1$ defines the overall energy scale of the confinement. The parameter β allows for tuning the confinement strength, while V_1 represents the saturation barrier height.

To ensure a finite confinement depth, the effective potential is defined as

$$V(x,y) = \begin{cases} g(x,y), & \text{if } g(x,y) < V_1 + g(h_k,0), \\ V_1 + g(h_k,0), & \text{otherwise}, \end{cases} \tag{3}$$

where

$$h_k = R_2 \sqrt{2 \ln\left(\frac{R_1}{R_2} \right)}. \tag{4}$$

This construction allows the system to smoothly evolve from a DQD configuration with a pronounced central barrier ($R_2 < R_1$) to an effective single quantum dot with a flat-bottom potential when $R_2 \to R_1$.

The confinement potential introduced in Eq. (3) is intended to provide an effective description of laterally coupled semiconductor QDs with smoothly varying confinement profiles. Similar effective double-dot potentials have been widely employed in theoretical studies of coupled QD systems because experimentally realized confinement landscapes generated through electrostatic gating, nanolithographic patterning, or compositional modulation are generally characterized by continuous spatial variations rather than abrupt interfaces. In the present model, the Gaussian modulation provides a convenient means to continuously control the central barrier and the effective coupling between the two confinement regions.

From a physical perspective, the parameter R_1 determines the global confinement length scale, whereas R_2 controls the width of the Gaussian modulation and therefore the effective interdot separation and tunneling coupling strength. In particular, the condition $R_2 < R_1$ generates a pronounced double-dot confinement profile with two spatially separated minima, while the limit $R_2 \to R_1$ progressively suppresses the central barrier and leads to a flat-bottom single-dot-like confinement regime. The parameter V_1 defines the characteristic confinement-energy scale, and the scaling factor β allows systematic tuning of the overall confinement amplitude. The selected parameter ranges are consistent with typical length and energy scales used in GaAs-based semiconductor QD systems and were chosen to ensure the presence of well-confined, low-lying electronic states, along with strong sensitivity to electric-field-induced localization, tunneling, and hybridization effects.

2.3. Coulomb impurity potential

The interaction between the electron and localized Coulomb impurity centers is introduced through the potential

$$V_{\mathrm{C}}(x,y) = -\frac{k_1 q_0}{4\pi\epsilon\epsilon_0} \frac{1}{\sqrt{(x-x_0)^2+y^2}} - \frac{k_2 q_0}{4\pi\epsilon\epsilon_0} \frac{1}{\sqrt{(x+x_0)^2+y^2}}, \tag{5}$$

where q_0 is the elementary charge, ϵ_0 is the vacuum permittivity, and ϵ is the static dielectric constant of the host material (in this work, $\epsilon = 12.58$, corresponding to the GaAs dielectric constant). The parameters k_1 and k_2 control the presence and symmetry of the Coulomb centers, while x_0 specifies their lateral positions along the x direction.

2.4. External electric field

An external in-plane electric field $\mathbf{F}$ is applied, forming an angle θ with respect to the x axis. The corresponding interaction potential is

$$V_{\mathrm{F}}(x,y) = q_0 \left(F_x x + F_y y \right), \tag{6}$$

with the field components given by

$$F_x = F\cos\theta, \qquad F_y = F\sin\theta, \tag{7}$$

where F denotes the electric field magnitude. This formulation allows us to explore the vectorial nature of the quantum-confined Stark effect by varying both the magnitude and orientation of the applied field.

2.5. Geometrical features of the confinement potential: minima and separation

An important advantage of the confinement model introduced in Eqs. (2)–(3) is that, for $R_2 < R_1$, the Gaussian modulation generates two equivalent lateral minima along the x axis (with $y = 0$), giving rise to an effective double-well (double quantum dot) profile. These minima are located at

$$(x_{\min}, y_{\min}) = \left(\pm R_2 \sqrt{2 \ln\left(\frac{R_1}{R_2}\right)},\ 0 \right), \tag{8}$$

and their depth is given by

$$V_{\min} = V_0 \frac{R_2^2}{R_1^2} \left[1 + 2 \ln\left(\frac{R_1}{R_2}\right) \right], \tag{9}$$

where $V_0 = \beta V_1$ sets the energy scale of the confinement.

The spatial separation between the two minima along the x direction follows directly from Eq. (8) as

$$\Delta x = 2|x_{\min}| = 2R_2 \sqrt{2 \ln\left(\frac{R_1}{R_2}\right)}. \tag{10}$$

Therefore, the inter-dot distance is controlled by the ratio R_1/R_2 rather than by R_2 alone. As R_2 increases toward R_1, the two minima approach the center, and the double-well character progressively disappears, leading to a single-dot-like confinement with a flat-bottom profile around $x = 0$.

In addition, the local stiffness of the confinement around each minimum can be quantified through the curvature of $g(x, 0)$ evaluated at $x = x_{\min}$,

$$\left. \frac{d^2 g(x,0)}{dx^2} \right|_{x = x_{\min}} = \frac{8V_0}{R_1^2} \ln\left(\frac{R_1}{R_2}\right), \tag{11}$$

which explicitly shows that the confinement strength decreases as $R_2 \to R_1$ due to the vanishing of $\ln(R_1/R_2)$. Consequently, the energy spacing between confined levels tends to compress in the flat-bottom limit, consistent with the weakening of the effective harmonic confinement around the minima.

2.6. Numerical method

The 2D Schrödinger equation (1), together with the confinement and external potentials defined in Eqs. (3)–(6), constitutes a partial differential eigenvalue problem that cannot be solved analytically and is therefore addressed numerically using the finite element method (FEM). All calculations were performed using the licensed commercial software *COMSOL Multiphysics*, within the effective-mass approximation, which enables an accurate and flexible treatment of complex confinement profiles, Coulomb interactions, and boundary conditions in low-dimensional semiconductor nanostructures. The computational domain was discretized using an unstructured adaptive triangular mesh specifically designed to resolve the spatial variations of the potential landscape and the corresponding electronic envelope wave functions. The final mesh consists of 10 633 vertices and 20 896 triangular elements, covering a total meshed area of approximately 1920 nm^2. Mesh quality was assessed using the obliquity metric provided by COMSOL, which yielded a minimum element quality of 0.659 and an average quality of 0.962, indicating a highly regular and well-conditioned discretization. The element-area ratio is 0.321, which ensures controlled mesh grading and allows local refinement in regions where the potential varies rapidly. Homogeneous Dirichlet boundary conditions were imposed by setting the wave function to zero at the edges of a sufficiently large simulation domain, thus avoiding spurious confinement effects. Additional mesh refinement tests confirmed that the low-lying eigenenergies converge with further increases in mesh density, validating the numerical accuracy and robustness of the adopted discretization.

The present theoretical description is based on the single-band effective-mass approximation (EMA), which is appropriate for semiconductor nanostructures in which the characteristic confinement lengths are significantly larger than the crystal lattice constant. Under these conditions, the electronic envelope functions vary smoothly over many unit cells, allowing the carrier dynamics to be accurately described through slowly varying envelope wave functions associated with the conduction-band edge. In the present work, the confinement dimensions and external electric-field strengths considered remain within the regime where intervalley coupling, strong band mixing, and nonparabolicity effects are expected to be negligible. Consequently, the applied electric field primarily induces Stark shifts, wave-function redistribution, and modifications of the tunneling coupling between confinement regions, all of which are well described within the effective-mass framework. Similarly, the Coulomb interaction introduced in Eq. (5) corresponds to shallow donor impurity centers embedded in a dielectric semiconductor environment. Due to dielectric screening, the impurity potential remains sufficiently smooth at the scale of the crystal lattice, preserving the validity of the envelope-function approximation. The effective-mass formalism has been extensively and successfully employed in previous studies of impurity states, Stark effects, and coupled semiconductor quantum dots, providing reliable descriptions of confined electronic spectra and localization phenomena under external perturbations [8,10,13,34].

Additional validation of the numerical implementation was performed through the analysis of physically well-established limiting cases of the confinement model. In the absence of Coulomb impurities and external electric fields, the calculated confined states

reproduce the expected behavior of symmetric coupled quantum-dot systems, including tunneling-induced level splitting and progressive spectral compression as the confinement evolves toward the flat-bottom regime. Likewise, the calculated Stark shifts, localization effects, and field-induced hybridization phenomena are fully consistent with the theoretical behavior previously reported for coupled semiconductor quantum dots and impurity-related confined states within the effective-mass approximation [8,10,13,17, 18,34]. These consistency checks support the numerical robustness and physical reliability of the finite-element implementation adopted in the present work.

Due to the combined presence of the nontrivial double parabolic confinement potential, Coulomb impurity interaction, and externally applied electric field, the eigenvalue problem defined by Eq. (1) does not admit analytical solutions. Consequently, the confined electronic wave functions are obtained numerically within the finite element framework. In the present work, the spatial properties of the confined states are therefore analyzed through the probability density distributions $|\psi_n(x, y)|^2$, which provide direct physical information about localization, nodal structure, tunneling coupling, and impurity-induced asymmetry [34,35].

3. Results and discussions

The confinement potential profiles shown in Fig. 1 correspond to the effective one-dimensional cut $V(x, y = 0)$ of the double parabolic quantum dot for different values of the geometrical parameter R_2, with the characteristic length R_1 kept fixed. Due to the even parity of the potential, all curves are symmetric with respect to $x = 0$. The parameter R_1 defines the overall spatial scale of the parabolic confinement and therefore sets the reference length against which the Gaussian modulation is measured. For $R_2 < R_1$, the Gaussian term generates a local maximum in the center of the structure, while two equivalent minima emerge at finite positions $\pm x_{\min}$, giving rise to a double-dot configuration. This condition is clearly fulfilled for $R_2 = 0.1$ nm and $R_2 = 5.0$ nm in Fig. 1, whereas the limiting case $R_2 = 10$ nm ($R_2 = R_1$) marks the transition toward a single-dot–like profile. The positions and depths of the lateral minima are governed by the interplay between the Gaussian width R_2 and the parabolic length scale R_1. The minima occur at $x_{\min} = \pm R_2\sqrt{2\ln(R_1/R_2)}$, explicitly showing that their separation is controlled by the ratio R_2/R_1 rather than by R_2 alone. The corresponding minimum potential energy is given by $V_{\min} = V_0(R_2^2/R_1^2)\left[1 + 2\ln(R_1/R_2)\right]$, where $V_0 = \beta V_1$, indicating that the depth of the wells decreases as R_1 increases for fixed R_2. Physically, larger values of R_1 lead to softer overall confinement, reducing both the curvature at the minima and the effective barrier height, while smaller R_1 values enhance localization and strengthen the double-dot character. A comparison between panels (a) and (b) of Fig. 1 highlights the role of the parameter β in controlling the overall energy scale of the confinement, while the parameter R_1 governs the geometric stiffness of the structure. Since the potential amplitude scales with $V_0 = \beta V_1$ and the characteristic curvature scales inversely with R_1^2, reducing β or increasing R_1 both act to lower the central barrier and weaken confinement, albeit through different physical mechanisms. As a result, the tunneling coupling between the two dots is expected to increase either when β is reduced or when R_1 is enlarged, leading to an enhanced splitting between the lowest symmetric and antisymmetric states. Therefore, Fig. 1 illustrates how the combined tuning of R_2, R_1, and β provides an efficient route to control the transition between weakly and strongly coupled double-dot regimes, with direct implications for the properties of the confined energy spectrum, analyzed in the following sections.

Panel (c) of Fig. 1 provides a three-dimensional visualization of the confinement potential for the representative case $R_1 = 10$ nm, $R_2 = 5$ nm, and $\beta = 1.0$, corresponding to an intermediate coupling regime between the strongly separated double-dot configuration and the flat-bottom single-dot-like limit. The 3D representation clearly illustrates the spatial topology of the confinement landscape, characterized by two lateral minima separated by a finite central barrier. In this regime, the coupling between the two confinement regions is sufficiently strong to allow electronic tunneling and wave-function hybridization, while the double-dot character of the structure is still preserved. The figure also highlights the smooth spatial variation of the confinement potential in both the x and y directions, emphasizing the anisotropic nature of the effective confinement profile. From a physical perspective, this intermediate configuration is particularly relevant because it represents the regime in which the competition among localization, tunneling coupling, and electric-field-induced redistribution of the electronic density is most pronounced, giving rise to the rich Stark and hybridization phenomena analyzed throughout the manuscript.

Fig. 2 presents the energies of the lowest confined electronic states as a function of the geometrical parameter R_2, for fixed $R_1 = 10$ nm, zero electric field, and in the absence of Coulomb interaction. The upper edge of the lower shaded region indicates the minimum of the confinement potential $V_{\min}$, while the energy gap between the two shaded regions corresponds to the barrier height V_1. As R_2 increases, the effective quantum wells become wider, and the confinement weakens, leading to a reduction in the quantization energy measured relative to the local minimum $E_n - V_{\min}$. This weakening of confinement is reflected in the discrete levels tending toward the upper edge of the lower shaded region, indicating that the states become progressively less confined within the wells. The apparent increase in absolute energy levels as R_2 increases must therefore be interpreted with caution. As demonstrated by the potential analysis in Fig. 1, the minimum of the confinement potential $V_{\min}$ itself increases with R_2 through its explicit dependence on the ratio R_2/R_1. Consequently, the entire energetic floor of the double-well structure shifts upward as R_2 grows, and the confined eigenvalues follow this upward shift even though the confinement is actually being reduced. In this sense, the upward trend of the curves in Fig. 2 is dominated by the increase of the potential minimum rather than by an enhancement of the confinement strength. A comparison between panels (a) and (b) of Fig. 2 highlights the effect of the scaling parameter β on this behavior. Since the overall amplitude of the confinement potential is proportional to $V_0 = \beta V_1$, reducing β lowers both the barrier height and the curvature of the wells. As a result, for $\beta = 0.5$ the quantization energies relative to $V_{\min}$ are further reduced, leading to a stronger accumulation of energy levels near the upper edge of the lower shaded region when compared to the case $\beta = 1.0$. These results confirm that the evolution of the confined spectrum with R_2 is governed by the combined action of the upward shift of the

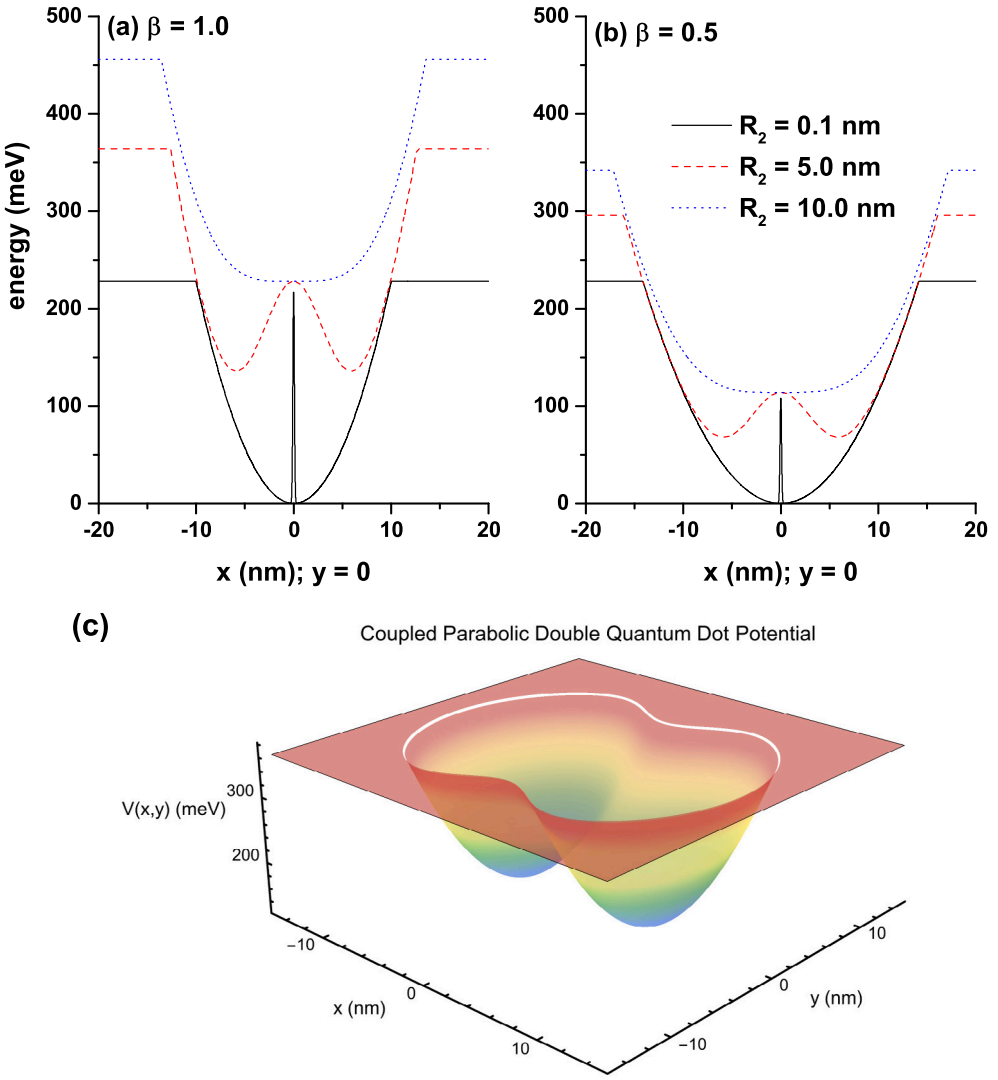


Fig. 1. Confinement potential profile $V(x, y = 0)$ along the x direction for a double parabolic quantum dot, calculated for different values of the geometrical parameter $R_2 = 0.1$, 5.0, and 10.0 nm, with $R_1 = 10$ nm kept fixed. Panels (a) and (b) correspond to $\beta = 1.0$ and $\beta = 0.5$, respectively. For large $|x|$, the potential saturates at $V_1 + g(h_k, 0)$, defining the effective barrier of the structure. Panel (c) presents a three-dimensional visualization of the confinement potential for the representative case $R_2 = 5$ nm and $\beta = 1.0$, illustrating the coupled double-well topology and the intermediate confinement regime characterized by a finite central barrier and partially coupled quantum dots.

potential minimum and the simultaneous weakening of the confinement, completely consistent with the physical picture established in Fig. 1.

Fig. 3 presents the energies of the lowest confined electronic states as a function of the scaling parameter β, for a fixed $R_1 = 10$ nm, zero electric field, and in the absence of Coulomb interaction. Panels (a) and (b) correspond to $R_2 = 3$ nm and $R_2 = 9$ nm, respectively, representing two distinct confinement regimes previously identified from the potential profiles in Fig. 1. Since the confinement potential amplitude scales as $V_0 = \beta V_1$, the minimum of the confinement potential depends linearly on β and is given by $V_{\min}(\beta) = \beta V_1 (R_2^2/R_1^2)\left[1 + 2\ln(R_1/R_2)\right]$. This explicit dependence implies that variations in β shift the entire energetic floor of the system, directly affecting the absolute energies of the confined states. The interpretation of the energy spectra in Fig. 3 therefore requires a clear distinction between absolute energies and quantization energies measured relative to the potential minimum. As β increases, the analytical expression for $V_{\min}$ predicts an upward displacement of the bottom of the wells, which is represented in the figure by the lower thick-green line. Consequently, confined energy levels shift upward and tend to accumulate near this boundary. At the same time, increasing β enhances the curvature of the confinement potential, leading to stronger localization and greater quantization energies $E_n - V_{\min}$. The combined action of these two effects explains both the monotonic increase in absolute energy levels and the progressive modification of the level spacing observed in Fig. 3. A direct comparison between panels (a) and (b) of Fig. 3 highlights how the influence of the scaling parameter β on the confined spectrum is strongly modulated by the geometric

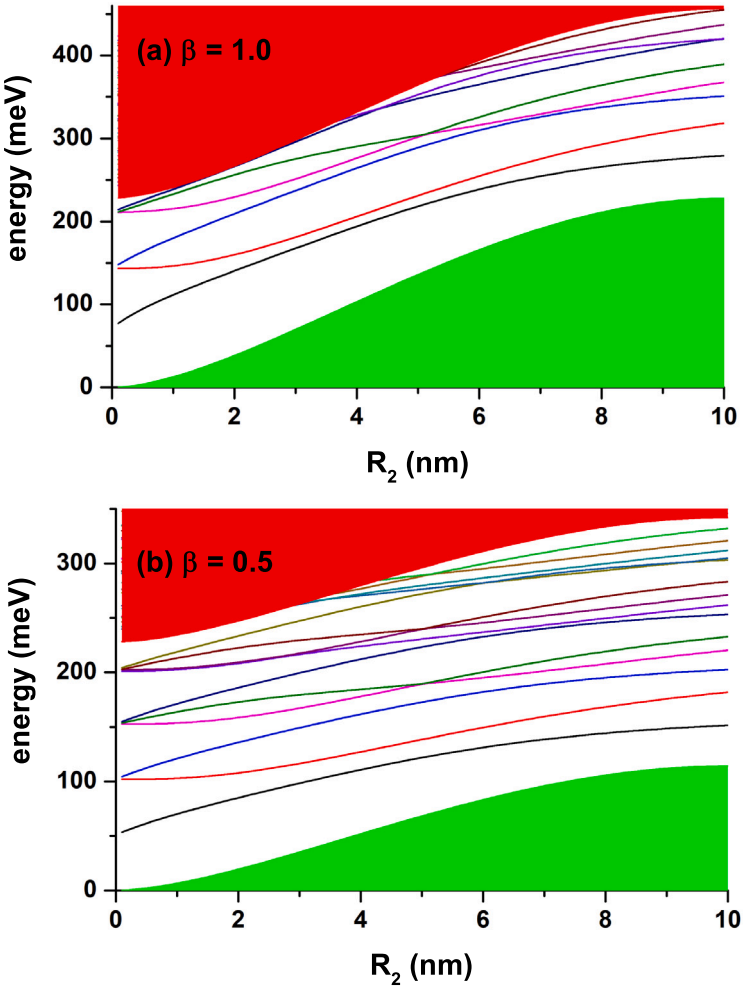


Fig. 2. Energies of the lowest confined states for an electron in a double quantum dot. The results are shown as a function of the parameter R_2, with $R_1 = 10$ nm, $F = 0$, and $k_1 = k_2 = 0$ kept fixed. Panels (a) and (b) correspond to $\beta = 1$ and $\beta = 0.5$, respectively. The upper edge of the lower shaded region indicates the minimum of the confinement potential, $V_{\min}$. The energy gap between the two shaded regions is fixed at $V_1 = 228$ meV.

parameter R_2 through its effect on the local stiffness of the confinement potential. For $R_2 = 3$ nm one obtains $V_{\min}(\beta) \simeq 0.070\,\beta$ meV, whereas for $R_2 = 9$ nm $V_{\min}(\beta) \simeq 0.224\,\beta$ meV; however, in both cases the separation between the potential minimum and the barrier height remains constant and equal to V_1 within the present model (note the constant energy separation between the two thick green and red lines). Consequently, the markedly different behavior observed in panels (a) and (b) cannot be attributed to changes in the effective well depth, but rather to the geometrical softening of the confinement as R_2 increases. This effect is quantified by the second derivative of the potential at the minimum,

$$\left.\frac{d^2 g(x,0)}{dx^2}\right|_{x=x_{\min}} = \frac{8V_0}{R_1^2}\ln\left(\frac{R_1}{R_2}\right), \tag{12}$$

which explicitly shows that the local curvature, and hence the effective confinement strength, decreases as R_2 approaches R_1 and vanishes in the limit $R_2 \to R_1$. As a result, within the harmonic approximation around each minimum, the quantization energies measured relative to the bottom of the well scale as $E_n - V_{\min} \sim \hbar\omega$, with $\omega \propto \sqrt{\ln(R_1/R_2)}$. Therefore, as R_2 increases and approaches R_1, the local curvature of the potential decreases, the characteristic frequency ω is reduced, and the energy spacing between confined levels becomes progressively smaller. This geometric softening of the confinement leads to a compression of the spectrum and the accumulation of energy levels near the lower thick line in Fig. 3(b), although the separation between the minimum and the barrier remains fixed. These results demonstrate that the evolution of the confined spectrum with β is governed by the interplay between the linear shift of the potential minimum and the simultaneous increase in the confinement strength, in full consistency with the potential analysis presented in Fig. 1.

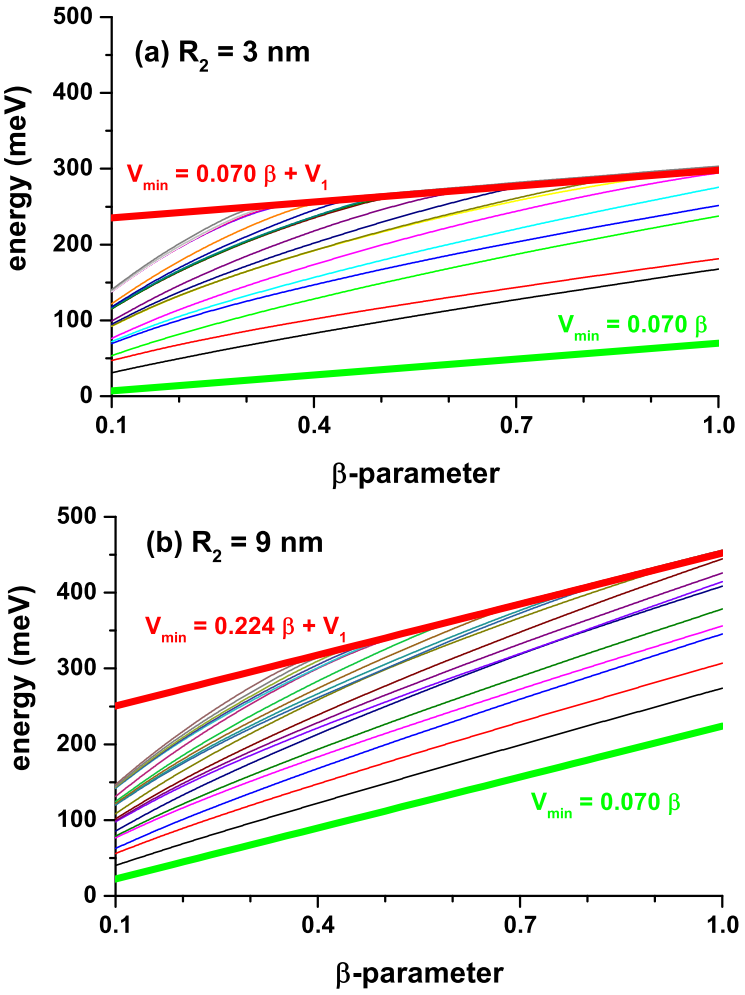


Fig. 3. Energies of the lowest confined states for an electron in a double quantum dot. The results are shown as a function of the parameter β, with $R_1 = 10$ nm, $F = 0$, and $k_1 = k_2 = 0$ kept fixed. Panels (a) and (b) correspond to $R_2 = 3$ nm and $R_2 = 9$ nm, respectively.

Fig. 4 illustrates the effect of the position of the impurity on the lowest confined energy levels of an electron in a double parabolic QD with an asymmetric Coulomb configuration ($k_1 = 1, k_2 = 0$), for two representative values of the geometric parameter R_2. In addition to the evolution of the energy spectrum, the figure includes probability density maps for the ground state and the three lowest excited states, which provide direct insight into the physical mechanisms underlying the observed energy shifts. For $R_2 = 3$ nm [Fig. 4(a)], the confinement potential exhibits a pronounced double-well character, leading to states that are either localized in one of the lateral minima or partially delocalized across the central barrier. The energy curves show a clear nonmonotonic dependence on the impurity position x_0, characterized by local minima and inflection points. This behavior can be directly correlated with the probability density distributions shown in the lower panels. When the impurity is located near the maxima of the probability density of a given state, the Coulomb attraction is maximized, resulting in a lowering of the corresponding energy level. In contrast, when the impurity is displaced toward regions of reduced probability density, the overlap between the electronic wave function and the impurity potential decreases, leading to weaker energy shifts. The probability density maps further reveal that the ground state remains predominantly localized within the lowest potential minimum, while the excited states exhibit more complex nodal structures and larger spatial extension. As a consequence, the excited-state energies are more sensitive to variations in x_0, displaying stronger nonmonotonic behavior and, in some cases, enhanced shifts compared to the ground state. In particular, the first and second excited states show pronounced changes in localization as the impurity moves from the center toward the outer regions of the structure, reflecting the competition between confinement-induced localization in the lateral wells and impurity-induced attraction. In contrast, for $R_2 = 9$ nm [Fig. 4(b)], the central barrier is strongly suppressed and the confinement potential approaches a flat-bottom single-dot-like regime. In this case, the energy levels exhibit a smoother, less strongly dependent behavior on the impurity position. The corresponding probability density distributions confirm that both the ground and excited states are more uniformly distributed throughout the confinement region, thereby reducing the sensitivity of the energy spectrum to the precise location of

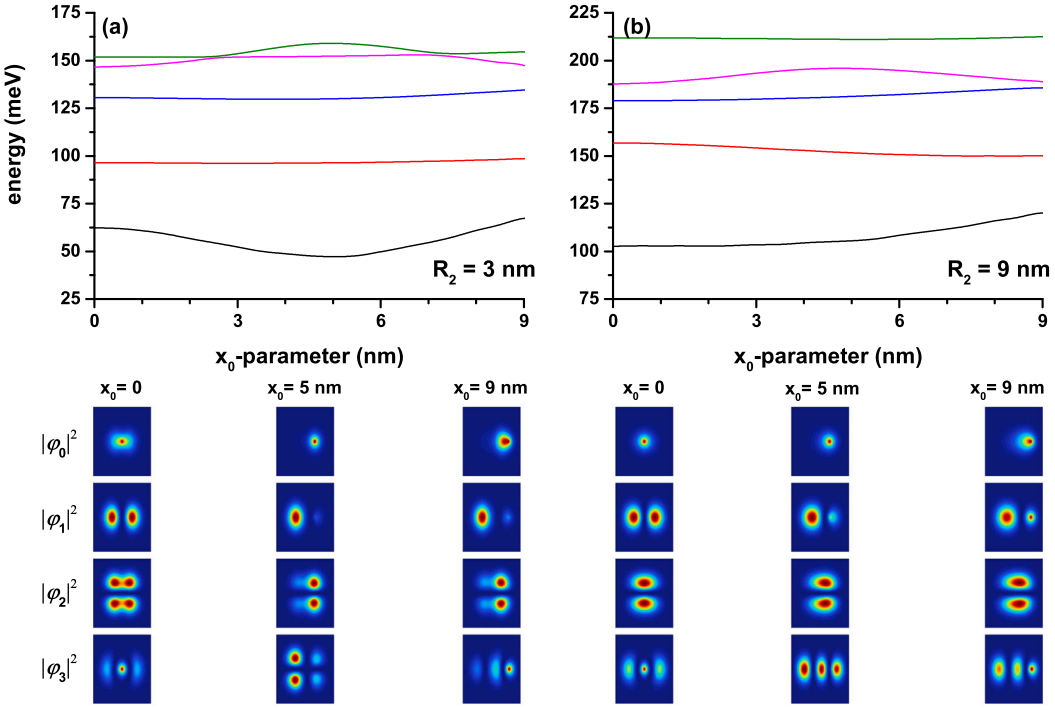


Fig. 4. Lowest confined energy levels of an electron in a double parabolic quantum dot as a function of the impurity-position parameter x_0, for $R_1 = 10$ nm, $\beta = 0.5$, $F = 0$, and an asymmetric Coulomb configuration ($k_1 = 1$, $k_2 = 0$). Panels (a) and (b) correspond to $R_2 = 3$ nm and $R_2 = 9$ nm, respectively. The upper panels display the energies of the ground state and the three lowest excited states as x_0 varies, while the lower panels show the corresponding probability density distributions $|\psi_n(x, y)|^2$ for the ground state ($n = 0$) and the first three excited states ($n = 1, 2, 3$), evaluated at three representative impurity positions: $x_0 = 0$, 5, and 9 nm.

the impurity. Although the impurity still induces measurable shifts, the absence of well-defined lateral minima limits the emergence of strong localization effects and suppresses the pronounced nonmonotonic features observed in the DQD regime. In general, the combined analysis of energy spectra and probability density maps in Fig. 4 demonstrates that impurity-induced modifications of the confined states are governed not only by the strength and position of the Coulomb potential, but also by the spatial structure of the electronic wave functions. The inclusion of probability density distributions thus provides a clear microscopic interpretation of the energy-level behavior and highlights the crucial role of wave-function localization in determining the response of DQD systems to impurity perturbations.

Fig. 5 presents the evolution of the lowest confined energy levels of an electron in a double parabolic QD as a function of the impurity-position parameter x_0 for a symmetric Coulomb configuration ($k_1 = k_2 = 1$), together with the corresponding probability density distributions of the ground state and the three lowest excited states. The inclusion of probability density maps provides a direct visualization of how the restoration of spatial symmetry influences both localization properties and impurity-induced energy shifts. For $R_2 = 3$ nm [Fig. 5(a)], the confinement potential retains a pronounced double-well character; however, the presence of two symmetrically placed Coulomb centers preserves inversion symmetry along the x direction. As a consequence, the energy levels exhibit smoother, more regular dependencies on x_0 than in the asymmetric case discussed in Fig. 4. The probability density distributions confirm that the electronic states remain either symmetrically localized in the lateral wells or delocalized across both minima, with no preferential localization toward a single side of the structure. When impurities are positioned near the maxima of the probability density, the Coulomb attraction enhances binding and lowers energy levels, but the symmetric overlap prevents the emergence of strongly nonmonotonic features. The probability maps further indicate that the ground state maintains a highly symmetric spatial profile for all impurity positions, while the excited states exhibit nodal structures consistent with their parity. Although these excited states are spatially more extended and therefore more sensitive to variations in x_0, the symmetric placement of the impurities ensures that the energy shifts remain balanced and nearly monotonic. This behavior contrasts sharply with the asymmetric configuration, in which impurity-induced symmetry breaking leads to pronounced changes in localization and enhanced energy-level modulation. In the case of $R_2 = 9$ nm [Fig. 5(b)], the confinement potential approaches a single-dot-like regime with a nearly flat bottom. The probability density distributions reveal that both the ground and excited states are broadly delocalized over the entire confinement region, further reducing the sensitivity of the energy spectrum to the precise impurity position. As a result, the energy levels display only weak variations with x_0, reflecting the reduced ability of the symmetrically distributed impurities to induce localization in the absence of a pronounced double-well structure. In this regime, the dominant effect of the impurities is to introduce a nearly uniform energy renormalization rather than to modify the spatial character of the confined states.

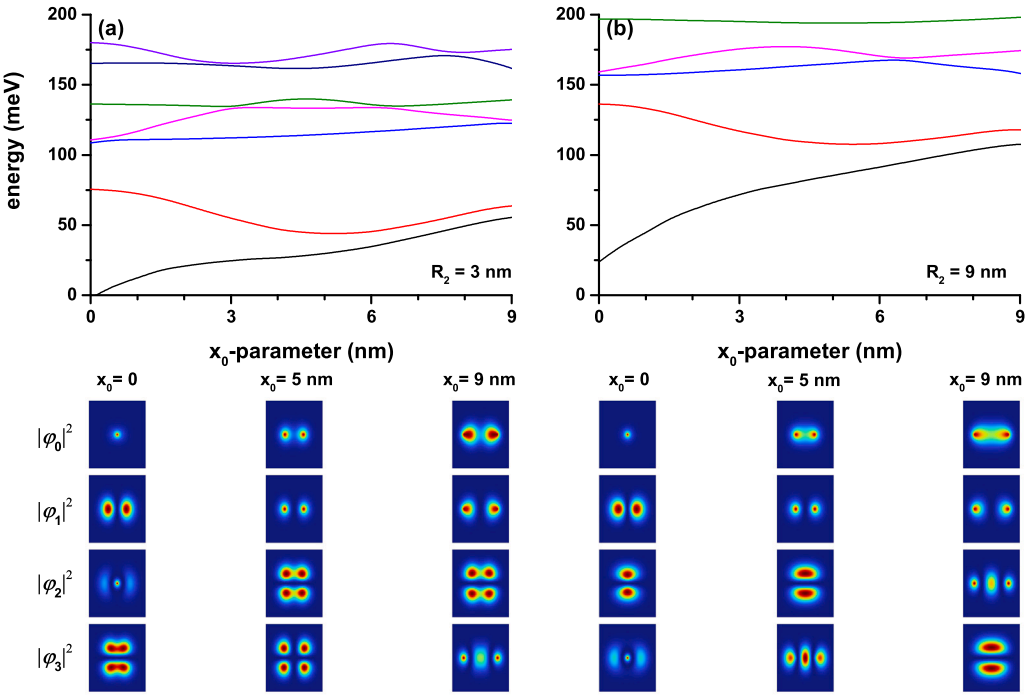


Fig. 5. Lowest confined energy levels of an electron in a double parabolic quantum dot as a function of the impurity-position parameter x_0, for $R_1 = 10$ nm, $\beta = 0.5$, $F = 0$, and a symmetric Coulomb configuration ($k_1 = k_2 = 1$). Panels (a) and (b) correspond to $R_2 = 3$ nm and $R_2 = 9$ nm, respectively. The upper panels show the evolution of the confined energy spectrum as the two Coulomb centers are symmetrically displaced along the x direction, while the lower panels present the probability density distributions $|\psi_n(x, y)|^2$ of the ground state and the three lowest excited states ($n = 0, 1, 2, 3$) for three selected impurity positions: $x_0 = 0$, 5, and 9 nm.

Consequently, the probability density maps exhibit smooth, spatially extended distributions with only minor distortions around the impurity locations. The combined analysis of energy spectra and probability density distributions highlights how impurity symmetry can be used as an additional control parameter to regulate the sensitivity of confined states to external perturbations, providing valuable insight for the design of robust QD-based devices.

Fig. 6 shows the evolution of the lowest confined electron energy levels as a function of the applied electric field for $\theta = 0$, i.e., $F_x = F$ and $F_y = 0$, in the presence of a single Coulomb center ($k_1 = 1$, $k_2 = 0$). Calculations are performed for $R_1 = 10$ nm and $\beta = 0.5$, considering four different combinations of the geometrical and impurity-position parameters (R_2, x_0). The response of each energy level to the electric field can be interpreted in terms of a quantum-confined Stark effect modified by impurity-induced asymmetry. In general, the field dependence of the nth confined state can be approximated as

$$E_n(F) \approx E_n(0) - p_n F - \frac{1}{2}\alpha_n F^2, \tag{13}$$

where $p_n = e\langle x\rangle_n$ represents an effective permanent dipole moment (i.e., a nonzero average electron displacement along the field direction in the absence of the external field due to structural or impurity-induced asymmetry), and α_n is the polarizability of the state (which quantifies the ability of the electronic wave function to deform and redistribute under the action of the electric field). In a symmetric confinement potential, p_n vanishes and the Stark shift is predominantly quadratic; however, the presence of an off-center Coulomb impurity breaks the inversion symmetry and gives rise to a finite linear contribution.

For $R_2 = 3$ nm [Figs. 6(a) and 6(b)], the confinement potential exhibits a pronounced central barrier, and the system behaves as a double quantum dot. In this regime, the applied electric field detunes the two lateral wells, favoring charge localization in one of them. As a consequence, the ground-state energy displays a strongly asymmetric and, in some cases, quasi-linear dependence on F, indicating the dominance of the linear Stark term associated with a nonzero dipole moment. This effect is particularly pronounced for $x_0 = 9$ nm [Fig. 6(b)], where the Coulomb center is located close to the lateral probability maximum and the electric field can either enhance or suppress the electron–impurity overlap depending on its orientation. The first excited state follows the same qualitative trend, but with a reduced sensitivity to F, reflecting its nodal structure and weaker localization, which limit the magnitude of both p_n and the effective impurity-induced energy shift. Higher excited states exhibit smoother, more symmetric curvatures, consistent with a larger contribution from the quadratic Stark term governed by their increased polarizability.

In contrast, for $R_2 = 9$ nm [Figs. 6(c) and 6(d)] the confinement potential develops a flat bottom and the central barrier is strongly suppressed, leading to a single quantum dot regime. In this case, the electric field mainly induces a continuous displacement and deformation of the electronic wave functions, resulting in a more regular Stark response. When the impurity is located near the

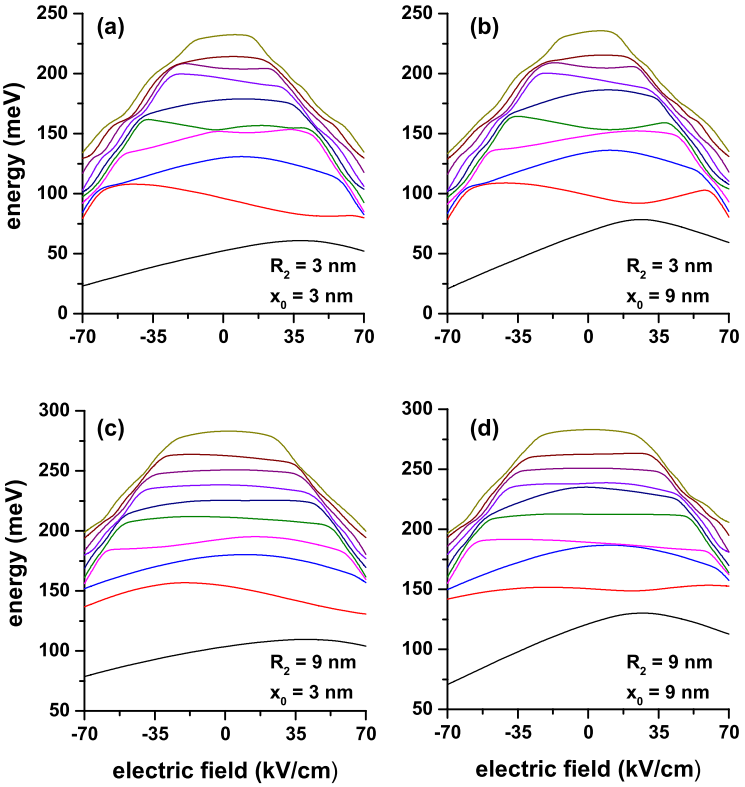


Fig. 6. Energies of the lowest confined states for an electron in a double quantum dot. The results are shown as a function of the applied electric field, with $R_1 = 10$ nm, $\theta = 0$, $\beta = 0.5$, $k_1 = 1$, and $k_2 = 0$ kept fixed. Several combinations of (R_2, x_0) nm have been considered: $(3,3)$ (a), $(3,9)$ (b), $(9,3)$ (c), and $(9,9)$ (d).

center ($x_0 = 3$ nm), the field dependence of the confined energies is predominantly quadratic, indicating that the polarizability term dominates. For $x_0 = 9$ nm, a finite asymmetry is introduced, and the ground state exhibits a mixed linear–quadratic behavior, although the overall sensitivity to F remains weaker than in the double quantum dot regime. The first excited state again shows a reduced curvature and weaker asymmetry compared to the ground state due to its broader spatial extension.

The behavior observed in Fig. 6 is fully consistent with the impurity-position effects discussed in Fig. 4, where variations in x_0 were shown to control the degree of electron localization through the overlap between the wave function probability maxima and the Coulomb center. In the presence of an external electric field, this mechanism is further enhanced by the field-induced redistribution of the electronic density. In general, Fig. 6 shows that the electric-field tunability of confined energy levels is strongly governed by the interplay between the central barrier, the emergence of a flat-bottom confinement, and the impurity-induced asymmetry, highlighting the crucial role of geometry and external fields in controlling the electronic structure of double quantum dot systems.

An additional important feature revealed in Fig. 6 is the appearance of an anticrossing between the ground state and the first excited state as the electric field is varied. This effect is particularly evident in panels (b) and (d), corresponding to $x_0 = 9$ nm, and is already hinted at in panels (a) and (c) for $x_0 = 3$ nm. The anticrossing arises from field-induced mixing of states with different localization characters when their energies approach each other. In the presence of an off-center Coulomb impurity, the electric field modifies the relative weight of the electronic wave function in different spatial regions, leading to a nonvanishing coupling matrix element between the ground and first excited states. As a result, instead of a true level crossing, the interaction produces an energy repulsion characterized by a minimum energy gap at a critical electric field. This behavior can be qualitatively understood within a two-level model, where the effective Hamiltonian on the basis of the unperturbed ground and first excited states reads

$$H_{\mathrm{eff}}(F) = \begin{pmatrix} E_0(F) & V_{01}(F) \\ V_{01}(F) & E_1(F) \end{pmatrix}, \tag{14}$$

with $V_{01}(F) = \langle \psi_0 | eFx | \psi_1 \rangle$ representing the field-induced coupling between the two states. When $E_0(F) \approx E_1(F)$, the coupling term reduces the degeneracy and produces the observed anticrossing. The effect is stronger in panels (b) and (d) because, for larger impurity displacement ($x_0 = 9$ nm), both states acquire a pronounced asymmetry and comparable spatial overlap in the vicinity of the impurity, which enhances off-diagonal coupling. In contrast, for smaller x_0 [panels (a) and (c)], the mixing is weaker, and the anticrossing manifests itself only as a slight avoided crossing. Overall, the presence of these anticrossings demonstrates that the

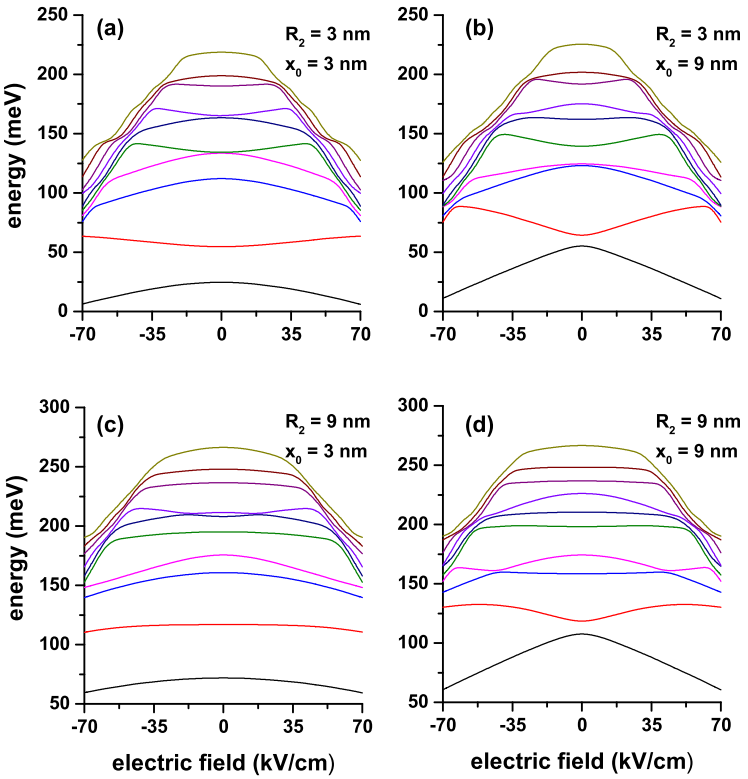


Fig. 7. Energies of the lowest confined states for an electron in a double quantum dot. The results are shown as a function of the applied electric field, with $R_1 = 10$ nm, $\theta = 0$, $\beta = 0.5$, $k_1 = 1$, and $k_2 = 1$ kept fixed. Several combinations of (R_2, x_0) nm have been considered: $(3,3)$ (a), $(3,9)$ (b), $(9,3)$ (c), and $(9,9)$ (d).

electric field not only shifts the confined energy levels but also actively controls the hybridization between the ground and first excited states, providing an additional mechanism for tuning the electronic structure in double quantum dot systems.

At high electric field magnitudes, an additional and physically significant feature emerges in Fig. 6, namely the accumulation (crowding) of excited states within a very narrow energy interval, particularly around $F \simeq -70$ kV/cm and $F \simeq +70$ kV/cm. This behavior reflects the dominance of the linear Stark term eFx over the intrinsic confinement potential, which strongly tilts the effective potential landscape along the field direction and reduces the effective confinement length. As the electric field approaches a critical value F_c, defined by the condition that the field-induced potential drop across the structure becomes comparable to the confinement depth, the spacing between higher excited levels progressively collapses. In this regime, the excited states, characterized by larger spatial extension and higher polarizability, are particularly sensitive to the field and experience a substantial redistribution of their probability density, leading to partial delocalization and enhanced tunneling toward the edges of the structure. Consequently, the discrete spectrum evolves into a dense quasi-continuum of closely spaced levels, which can be interpreted as a precursor to field-induced ionization or to escape from the confinement region. This effect is further enhanced in configurations with reduced central barrier or strong impurity-induced asymmetry, where the competition between confinement, Coulomb attraction, and the external electric field becomes more pronounced. From a physical perspective, the accumulation of excited states at large F indicates a substantial modification of the confined electronic spectrum, which may have important implications for future studies of field-dependent optical and transport properties in coupled quantum-dot systems.

Fig. 7 depicts the evolution of the lowest confined electron energy levels as a function of the applied electric field for $\theta = 0$, i.e., $F_x = F$ and $F_y = 0$, in the presence of two symmetrically located Coulomb centers ($k_1 = k_2 = 1$). Calculations are performed for $R_1 = 10$ nm and $\beta = 0.5$, considering four different combinations of geometrical parameters and impurity-positions: $(R_2, x_0) = (3,3)$ in panel (a), $(3,9)$ in panel (b), $(9,3)$ in panel (c), and $(9,9)$ in panel (d). In contrast to Fig. 6, where the electronic spectrum is strongly affected by impurity-induced asymmetry, the symmetric arrangement of the Coulomb centers in Fig. 7 restores global inversion symmetry, leading to a qualitatively different Stark response.

Under these conditions, the effective permanent dipole moment of the confined states vanishes, $p_n = e\langle x\rangle_n = 0$, and the electric-field dependence of the energy levels is predominantly governed by the quadratic term of the quantum-confined Stark effect,

$$E_n(F) \simeq E_n(0) - \frac{1}{2}\alpha_n F^2, \tag{15}$$

where α_n denotes the polarizability of the nth state, which measures the ability of the electronic wave function to deform and redistribute under the action of the external field. As a consequence, the energy curves shown in Fig. 7 are largely symmetric with respect to $F = 0$, in clear contrast with the strongly asymmetric behavior observed in Fig. 6.

For $R_2 = 3$ nm [panels (a) and (b)], the confinement potential exhibits a pronounced central barrier, and the system operates in a well-defined DQD regime. In this case, the applied electric field symmetrically detunes the two lateral wells and induces a redistribution of the electronic probability density between them. The ground-state energy displays a clearly parabolic dependence on F, with a maximum at zero field, consistent with a predominantly quadratic quantum-confined Stark effect, $E_0(F) \simeq E_0(0) - \frac{1}{2}\alpha_0 F^2$. The excited states exhibit progressively weaker curvature as their energy increases, reflecting increased polarizability due to their larger spatial extent. A comparison between panels (a) and (b) reveals that increasing the impurity displacement from $x_0 = 3$ nm to $x_0 = 9$ nm enhances the coupling between the electric field and the confined states, as the Coulomb centers approach the lateral probability maxima, resulting in a stronger compression of the excited-state spectrum at high electric fields. When $R_2 = 9$ nm [panels (c) and (d)], the central barrier is strongly suppressed and the confinement potential develops a flat-bottom profile, leading to a single quantum dot regime. In this configuration, the electric field mainly produces a continuous polarization of the electronic states without inducing abrupt changes in localization. The ground state exhibits a smooth, nearly ideal quadratic Stark shift, while the excited states remain closely spaced in energy, especially at large field magnitudes. The effect of the impurity position is less pronounced than in the double quantum dot regime, but for $x_0 = 9$ nm [panel (d)] the increased separation between the Coulomb centers and the geometric center of the structure leads to a larger effective polarizability and enhances the field-induced compression of the excited-state spectrum.

A common feature observed in all panels of Fig. 7 is the accumulation of excited states within a narrow energy interval at high electric field magnitudes, particularly for $|F| \gtrsim 70$ kV/cm. This accumulation can be attributed to the dominance of the field-induced potential tilt over intrinsic confinement, which reduces the effective confinement length and collapses the energy spacing between higher-excited states. Physically, this behavior signals a transition from a discrete spectrum with well-separated levels to a dense quasi-continuum, which can be regarded as a precursor to field-assisted tunneling or ionization. The effect is more pronounced for excited states due to their larger spatial extension and higher polarizability. Overall, Fig. 7 demonstrates that, in the presence of symmetrically distributed Coulomb centers, the electric-field response of the confined energy levels is primarily controlled by the polarizability of the electronic states and by the topology of the confinement potential. The restoration of inversion symmetry suppresses linear Stark contributions and enables clear identification of the roles of the central barrier and flat-bottom confinement in shaping the electronic spectrum, may be useful for future studies of field-controlled electronic and transport phenomena in coupled QD systems.

Fig. 8 displays the dependence of the lowest confined electron energy levels on the orientation angle θ of the applied electric field, while keeping its magnitude fixed at $F = 60$ kV/cm. The field components are given by $F_x = F\cos\theta$ and $F_y = F\sin\theta$, allowing a systematic analysis of the directional anisotropy of the Stark response. The calculations are performed for $R_1 = 10$ nm and $\beta = 0.5$, considering an asymmetric Coulomb configuration with a single impurity center ($k_1 = 1$, $k_2 = 0$). Four combinations of the geometrical and impurity-position parameters are analyzed: $(R_2, x_0) = (3, 3)$ in panel (a), $(3, 9)$ in panel (b), $(9, 3)$ in panel (c), and $(9, 9)$ in panel (d). The angular dependence observed in Fig. 8 originates from the intrinsic anisotropy of the confinement potential and from the preferential localization of the Coulomb impurity along the x direction. The interaction with the electric field,

$$V_F = eF_x x + eF_y y = eF(x\cos\theta + y\sin\theta), \tag{16}$$

projects the external perturbation onto directions with different confinement strengths, leading to an orientation-dependent redistribution of the electronic probability density. As a result, the confined energy levels exhibit nontrivial modulations as θ varies, even though the field magnitude remains constant.

From a physical perspective, the angular dependence of the Stark effect originates from the anisotropic coupling between the in-plane electric field and the spatial distribution of the confined electronic states. From Eq. (16), it is observed that the effective Stark interaction depends on the projection of the electric field along the principal confinement directions. Because the double parabolic quantum-dot system exhibits a nonuniform confinement topology and spatially anisotropic wave-function distributions, the response of the confined states becomes strongly dependent on the field orientation. When the electric field is aligned predominantly along the interdot axis, it modifies the tunneling coupling and charge redistribution between the two confinement regions, resulting in stronger Stark shifts and enhanced hybridization. In contrast, for field orientations with larger transverse components, the coupling to the interdot degree of freedom weakens, reducing energy-level sensitivity. In addition, the presence of Coulomb impurities introduces local symmetry breaking, which further enhances the angular dependence of the Stark response by generating anisotropic effective dipole moments and nonuniform spatial polarization of the electronic density. As a consequence, the angular modulation of the confined energy spectrum reflects the combined influence of confinement anisotropy, impurity-induced asymmetry, and field-direction-dependent hybridization between localized electronic states.

For $R_2 = 3$ nm [panels (a) and (b)], the confinement potential exhibits a pronounced central barrier, and the system operates in a double quantum dot regime. In this case, the angular dependence of the ground-state energy is clearly nonmonotonic, with well-defined maxima and minima associated with orientations of the electric field that either enhance or suppress the overlap between the electronic wave function and the impurity located at x_0. When the field is oriented close to $\theta = 0°$ or $180°$, its projection along the x direction dominates and efficiently drives charge redistribution between the two lateral wells. In contrast, for $\theta \approx 90°$ the field acts mainly along the y direction, where the confinement is stronger, and the impurity-induced asymmetry is less effective, resulting in reduced energy modulation. Increasing the impurity displacement to $x_0 = 9$ nm [panel (b)] amplifies this angular sensitivity, as the electric field can more efficiently align or misalign the electronic probability maxima with the Coulomb center.

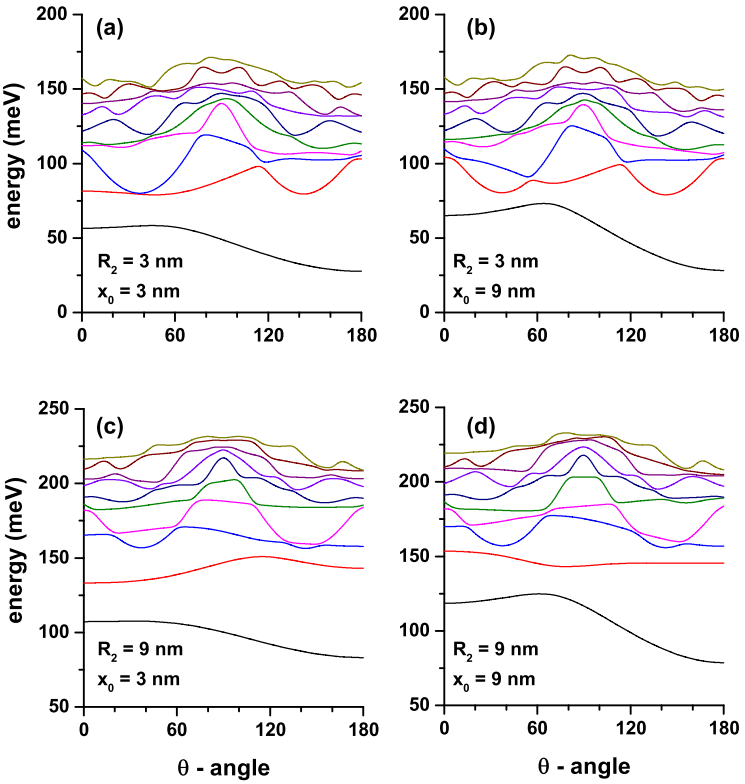


Fig. 8. Energies of the lowest confined states for an electron in a double quantum dot. The results are shown as a function of the applied electric field, with $R_1 = 10$ nm, $\theta = 0$, $\beta = 0.5$, $k_1 = k_2 = 1$ kept fixed. Several combinations of (R_2, x_0) nm have been considered: $(3,3)$ (a), $(3,9)$ (b), $(9,3)$ (c), and $(9,9)$ (d).

When $R_2 = 9$ nm [panels (c) and (d)], the central barrier is strongly suppressed, and the confinement potential develops a flat-bottom profile characteristic of a single QD regime. In this case, the angular dependence of the energy levels becomes smoother and more regular, reflecting a predominantly continuous polarization of the electronic states rather than abrupt changes in localization.

The excited states in Fig. 8 exhibit a richer angular structure than the ground state, due to their nodal patterns and larger spatial extension. Their energies show multiple extrema as a function of θ, indicating interference between different regions of the probability density under field-induced rotation of the polarization direction. This behavior is especially pronounced in the double quantum dot regime, where the coexistence of two lateral confinement regions introduces competing spatial scales.

The angular tunability of the confined energy levels has direct implications for the system's intraband optical absorption. In the intraband regime, optical transitions occur between different confined electronic states within the same band, and the absorption coefficient is proportional to the square of the intraband dipole matrix element

$$\mathcal{M}_{nn'} \propto \left|\langle \psi_n | \hat{\mathbf{e}} \cdot \mathbf{r} | \psi_{n'} \rangle\right|^2, \tag{17}$$

where ψ_n and $\psi_{n'}$ denote the initial and final confined electronic states, respectively, and $\hat{\mathbf{e}}$ is the polarization vector of the incident radiation. The orientation of the external electric field induces a redistribution of the electronic probability density and modifies the spatial symmetry of the confined states, which directly affects both the magnitude and the angular dependence of the intraband transition matrix elements. In particular, changes in the field orientation alter the relative contributions of the x and y components of the dipole operator, leading to a selective enhancement or suppression of intraband transitions depending on the polarization direction. As a consequence, the angular modulation of the electronic spectrum observed in Fig. 8 is expected to manifest as a pronounced anisotropy in the intraband absorption spectra, with orientation-dependent transition energies and oscillator strengths, thereby providing an efficient mechanism for tuning the intraband optical response through control of the external-field direction.

Overall, Fig. 8 demonstrates that the orientation of the electric field provides an additional, powerful degree of freedom for controlling not only the confined energy levels but also the intraband optical properties of double quantum dot systems. The combined effect of confinement anisotropy, impurity-induced asymmetry, and field orientation highlights the fundamentally vectorial nature of the Stark effect in low-dimensional semiconductor nanostructures and opens the possibility of tailoring intraband absorption spectra, oscillator strengths, and angular selection rules through external-field engineering.

Fig. 9 shows the angular dependence of the lowest confined electron energy levels for a fixed electric field magnitude $F = 60$ kV/cm, considering a symmetric Coulomb configuration with two impurity centers ($k_1 = k_2 = 1$). The field orientation is defined

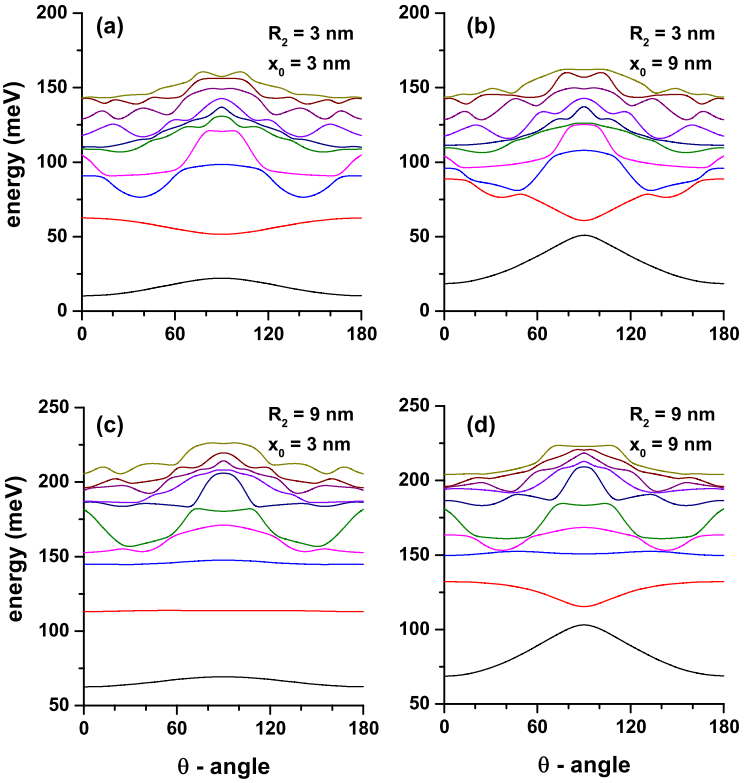


Fig. 9. Energies of the lowest confined states for an electron in a double quantum dot. The results are shown as a function of the θ-angle, with $R_1 = 10$ nm, $F = 60$ kV/cm, $\beta = 0.5$, and $k_1 = k_2 = 1$ kept fixed. Several combinations of (R_2, x_0) nm have been considered: $(3,3)$ (a), $(3,9)$ (b), $(9,3)$ (c), and $(9,9)$ (d).

through $F_x = F\cos\theta$ and $F_y = F\sin\theta$, allowing the analysis of the vectorial nature of the Stark response. The calculations are performed for $R_1 = 10$ nm and $\beta = 0.5$, and four combinations of the geometrical and impurity-position parameters are considered: $(R_2, x_0) = (3,3)$ in panel (a), $(3,9)$ in panel (b), $(9,3)$ in panel (c), and $(9,9)$ in panel (d). Unlike the asymmetric case analyzed in Fig. 8, the symmetric distribution of the Coulomb centers restores global inversion symmetry, which has important consequences for the angular Stark behavior. Due to the symmetric Coulomb configuration, the effective permanent dipole moment of the confined states vanishes, $p_n = e\langle x\rangle_n = 0$, and the angular dependence of the energy levels is governed predominantly by polarization effects. As a result, the confined energies exhibit smooth and globally symmetric variations with respect to θ, reflecting the quadratic nature of the Stark response and the anisotropic polarizability of the electronic states rather than linear field-induced shifts.

For $R_2 = 3$ nm [panels (a) and (b)], the confinement potential exhibits a pronounced central barrier, leading to a well-defined double quantum dot regime. In this configuration, the angular dependence of the ground-state energy displays a clear maximum around $\theta \simeq 90°$, corresponding to a field orientation mainly along the y direction, where the confinement is stronger. For $\theta \simeq 0°$ and 180°, the electric field is aligned with the x axis, promoting a symmetric polarization of the electronic density toward the lateral regions. Increasing the impurity displacement from $x_0 = 3$ nm to $x_0 = 9$ nm enhances the amplitude of the angular modulation, as the Coulomb centers approach the lateral probability maxima, thereby increasing the sensitivity of the states to the field orientation even under conditions of restored symmetry. When $R_2 = 9$ nm [panels (c) and (d)], the central barrier is strongly suppressed, and the confinement potential develops a flat-bottom profile characteristic of a single quantum dot regime. In this case, the angular dependence of the energy levels becomes smoother and more regular, reflecting a continuous polarization of the electronic wave functions rather than abrupt changes in localization. The effect of the impurity position is weaker than in the double quantum dot regime; however, for $x_0 = 9$ nm, the increased spatial separation between the Coulomb centers and the structure's centerthe enhances the polarizability, producing a more pronounced yet still symmetric angular modulation. The excited states in Fig. 9 exhibit a richer angular structure than the ground state due to their nodal patterns and larger spatial extension. Their energies show multiple maxima and minima as a function of θ, indicating interference between different spatial regions of the probability density under rotation of the electric field direction. Although the symmetric Coulomb configuration prevents angular asymmetry, it does not suppress these oscillatory features, which are intrinsic to the anisotropic polarizability of the excited states.

The angular modulation of the confined energy spectrum observed in Fig. 9 has direct implications for the intraband optical absorption of the system. The intraband absorption coefficient for a transition between two confined states n and n' can be written

as

$$\alpha_{nn'}(\theta) \propto \left|\langle\psi_n|\hat{\mathbf{e}}\cdot\mathbf{r}|\psi_{n'}\rangle\right|^2 \delta\left(E_{n'}(\theta)-E_n(\theta)-\hbar\omega\right), \tag{18}$$

where $\hat{\mathbf{e}}$ is the polarization vector of the incident radiation. Since both the transition energies $E_{n'}(\theta) - E_n(\theta)$ and the spatial symmetry of the wave functions depend explicitly on the field orientation, the intraband absorption spectra are expected to exhibit a pronounced angular dependence. In particular, the anisotropic polarization induced by the electric field modifies the relative contributions of the x and y components of the dipole operator, leading to orientation-dependent oscillator strengths and selection rules. Consequently, the angular control of the electric field provides a powerful mechanism to tune intraband absorption intensities and spectral positions, even in the presence of global spatial symmetry.

Overall, Fig. 9 demonstrates that, for symmetrically distributed Coulomb centers, the angular Stark response of the confined electronic spectrum is governed by the topology of the confinement potential and by the anisotropic polarizability of the states. The orientation of the electric field acts as a vectorial control parameter capable of modulating both the electronic spectrum and the intraband optical absorption coefficients $\alpha_{nn'}(\theta)$, highlighting the potential of angular field engineering for the design of tunable intraband optoelectronic devices based on double quantum dot systems.

4. Conclusions

In this work, we have carried out a detailed theoretical analysis of the electronic structure of a double parabolic quantum dot in the presence of external electric fields and Coulomb impurities. By systematically varying the geometrical parameter R_2, the impurity position x_0, the number and symmetry of Coulomb centers, as well as the magnitude and orientation of the applied electric field, we have identified the main physical mechanisms governing the confined energy spectrum.

Our results demonstrate that the confinement geometry plays a decisive role in determining the system's electronic regime. For small values of R_2, the emergence of a pronounced central barrier leads to clear double quantum dot behavior, characterized by strong localization, enhanced sensitivity to external fields, and the appearance of level repulsion and anticrossings between the ground and first excited states. In contrast, for larger R_2 values, the suppression of the central barrier yields a flat-bottom confinement profile, in which the system behaves as an effective single quantum dot with smoother Stark shifts and reduced sensitivity to impurity-induced asymmetry.

The application of an external electric field gives rise to the quantum-confined Stark effect, whose characteristics strongly depend on the symmetry of the impurity configuration. When the Coulomb centers are asymmetrically distributed, a finite permanent dipole moment is induced, leading to linear Stark contributions and strongly asymmetric energy shifts. In symmetric impurity configurations, inversion symmetry is restored, and the Stark response becomes predominantly quadratic, governed by the anisotropic polarizability of the confined states. At sufficiently high electric field magnitudes, an accumulation of excited states within narrow energy intervals is observed, indicating a transition toward a dense spectrum associated with enhanced tunneling and incipient field-assisted delocalization.

An important outcome of this study is the identification of the fundamentally vectorial nature of the Stark effect in double quantum dot systems. By varying the orientation of the electric field at a fixed magnitude, we have shown that the confined energy levels exhibit a pronounced angular dependence that reflects both the anisotropy of the confinement potential and the spatial distribution of the Coulomb impurities. This angular tunability persists even in symmetrically doped structures, where it arises from directional differences in electronic polarizability rather than from structural asymmetry.

Although optical properties are not explicitly addressed in the present work, the strong control of the electronic spectrum achieved through the magnitude and orientation of the electric field suggests several potential implications for future optical studies. In particular, the tunability of level spacings, the occurrence of anticrossings, and the angular modulation of the confined states are expected to play a crucial role in determining intraband transition energies, oscillator strengths, and angular selection rules in low-dimensional semiconductor nanostructures.

Overall, the results presented here highlight the rich interplay between confinement geometry, impurity configuration, and external electric fields in double quantum dot systems. The ability to engineer the electronic spectrum through both scalar and vectorial control parameters provides a robust physical platform for future investigations into transport and optical phenomena in electrically tunable quantum-confined systems.

CRediT authorship contribution statement

E. Kasapoglu: Writing – review & editing, Writing – original draft, Investigation, Conceptualization. **Melike Behiye Yücel:** Writing – review & editing, Writing – original draft, Investigation. **C.A. Duque:** Visualization, Investigation.

Declaration of competing interest

The authors declare that they have no known competing financial interests or personal relationships that could have appeared to influence the work reported in this paper.

Acknowledgments

CAD is grateful to Colombian agencies CODI-Universidad de Antioquia (project "Nanoestructuras semiconductoras con simetría axial basadas en InAs y GaAs para aplicaciones en electrónica ultra e hiperrápida") and Facultad de Ciencias Exactas y Naturales-Universidad de Antioquia (CAD exclusive dedication project 2026–2027).

Data availability

Data will be made available on request.

References

[1] J. Shen, Y. Zhu, X. Yang, C. Li, Graphene quantum dots: emergent nanolights for bioimaging, sensors, catalysis and photovoltaic devices, Chem. Commun. 48 (2012) 3686, http://dx.doi.org/10.1039/C2CC00110A.
[2] H. Sun, L. Wu, W. Wei, X. Qu, Recent advances in graphene quantum dots for sensing, Mater. Today 16 (2013) 433, http://dx.doi.org/10.1016/j.mattod.2013.10.020.
[3] T. Yuan, T. Meng, P. He, Y. Shi, Y. Li, X. Li, L. Fan, S. Yang, Carbon quantum dots: an emerging material for optoelectronic applications, J. Mater. Chem. C 7 (2019) 6820, http://dx.doi.org/10.1039/C9TC01730E.
[4] S. Kabi, A.G.U. Perera, Effect of quantum dot size and size distribution on the intersublevel transitions and absorption coefficients of III–V semiconductor quantum dots, J. Appl. Phys. 117 (2015) 124303, http://dx.doi.org/10.1063/1.491637218.
[5] L.O. Cinteza, Quantum dots in biomedical applications: advances and challenges, J. Nanophotonics 4 (2010) 042503, http://dx.doi.org/10.1117/1.3500388.
[6] O.E. Semonin, J.M. Luther, M.C. Beard, Quantum dots for next-generation photovoltaics, Mater. Today 15 (2012) 508, http://dx.doi.org/10.1016/S1369-7021(12)70220-1.
[7] F. Pisanello, L. Martiradonna, G. Lemenager, P. Spinicelli, A. Fiore, L. Manna, J.P. Hermier, R. Cingolani, E. Giacobino, M. De Vittorio, A. Bramati, Room temperature-dipolelike single photon source with a colloidal dot-in-rod, Appl. Phys. Lett. 96 (2010) 033101, http://dx.doi.org/10.1063/1.3291849.
[8] S.M. Reimann, M. Manninen, Electronic structure of quantum dots, Rev. Modern Phys. 74 (2002) 1283, http://dx.doi.org/10.1103/RevModPhys.74.1283.
[9] F.J. Kaiser, S. Kohler, P. Hänggi, M. Malecha, J. Ebbecke, A. Wixforth, H.W. Schumacher, B. Kästner, D. Reuter, A.D. Wieck, Theoretical and experimental investigations of Coulomb blockade in coupled quantum dot systems, J. Phys. : Condens. Matter 20 (2008) 374108, http://dx.doi.org/10.1088/0953-8984/20/37/374108.
[10] S.I. Pokutnyi, L. Jacak, J. Misiewicz, W. Salejda, G.G. Zegrya, Stark effect in semiconductor quantum dots, J. Appl. Phys. 96 (2004) 1115, http://dx.doi.org/10.1063/1.1759791.
[11] T.G. Pedersen, Stark effect and polarizability of graphene quantum dots, Phys. Rev. B 96 (2017) 115432, http://dx.doi.org/10.1103/PhysRevB.96.115432.
[12] R. Boussetta, O. Mommadi, A. El Moussaouy, M. Hbibi, S. Chouef, C.A. Duque, A. Kerkour El-Miad, Effect of the electric field orientation on stark shift, dipole moment and electronic properties in a circular toroidal quantum ring: Presence of shallow donor impurity, Phys. B 690 (2024) 416263, http://dx.doi.org/10.1016/j.physb.2024.416263.
[13] E. Räsänen, J. Könemann, R.J. Haug, M.J. Puska, R.M. Nieminen, Impurity effects in quantum dots: Toward quantitative modeling, Phys. Rev. B 70 (2004) 115308, http://dx.doi.org/10.1103/PhysRevB.70.115308.
[14] E.B. Al, E. Kasapoglu, H. Sari, I. Sökmen, Optical properties of spherical quantum dot in the presence of donor impurity under the magnetic field, Phys. B 613 (2021) 412874, http://dx.doi.org/10.1016/j.physb.2021.412874.
[15] K. Hasanirokh, A. Radu, C.A. Duque, Donor impurity in CdS/ZnS spherical quantum dots under applied electric and magnetic fields, Nanomaterials 12 (2022) 4014, http://dx.doi.org/10.3390/nano12224014.
[16] S. Sakiroglu, H. Sari, Contribution of the impurity to the thermodynamic properties of a quantum dot with a Gaussian confinement potential, Eur. Phys. J. Plus 140 (2025) 627, http://dx.doi.org/10.1140/epjp/s13360-025-06580-x.
[17] W.G. van der Wiel, S. De Franceschi, J.M. Elzerman, T. Fujisawa, S. Tarucha, L.P. Kouwenhoven, Electron transport through double quantum dots, Rev. Modern Phys. 75 (2002) 1, http://dx.doi.org/10.1103/RevModPhys.75.1.
[18] H. Zheng, J. Zhang, R. Berndt, A minimal double quantum dot, Sci. Rep. 7 (2017) 10764, http://dx.doi.org/10.1038/s41598-017-10814-z.
[19] Q.H. Wang, K. Kalantar-Zadeh, A. Kis, J.N. Coleman, M.S. Strano, Electronics and optoelectronics of two-dimensional transition metal dichalcogenides, Nat. Nanotechnol. 7 (2012) 699, http://dx.doi.org/10.1038/nnano.2012.193.
[20] S. Ahmed, J. Yi, Two-dimensional transition metal dichalcogenides and their charge carrier mobilities in field-effect transistors, Nano-Micro Lett. 9 (2017) 50, http://dx.doi.org/10.1007/s40820-017-0152-6.
[21] X. Liu, M.C. Hersam, 2D materials for quantum information science, Nat. Rev. Mater. 4 (2019) 669, http://dx.doi.org/10.1038/s41578-019-0136-x.
[22] A. Raja, A. Chaves, J. Yu, G. Arefe, H.M. Hill, A.F. Rigosi, T.C. Berkelbach, P. Nagler, C. Schüller, T. Korn, C. Nuckolls, J. Hone, L.E. Brus, T.F. Heinz, D.R. Reichman, A. Chernikov, Coulomb engineering of the bandgap and excitons in two-dimensional materials, Nat. Commun. 8 (2017) 15251, http://dx.doi.org/10.1038/ncomms15251.
[23] A. Chaves, J.G. Azadani, H. Alsalman, R. Frisenda D.R. da Costa, A.J. Chaves, S.H. Song, Y.D. Kim, D. He, J. Zhou, A. Castellanos-Gomez, F.M. Peeters, Z. Liu, C.L. Hinkle, S.-H. Oh, P.D. Ye, S.J. Koester, Y.H. Lee, Ph. Avouris, X. Wang, T. Low, Bandgap engineering of two-dimensional semiconductor materials, Npj 2D Mater. Appl. 4 (2020) 29, http://dx.doi.org/10.1038/s41699-020-00162-4.
[24] N.Y. Yengibaryan, G.A. Mantashian, T.A. Sargsian, C. Garoufalis, S. Baskoutas, D.B. Hayrapetyan, Tuning the electronic and optical properties of dumbbell quantum dot via electric field, Heliyon 11 (2025) e43395, http://dx.doi.org/10.1016/j.heliyon.2025.e43395.
[25] M. Jaouane, R. Arraoui, A. Fakkahi, A. Ed-Dahmouny, H. Azmi, K. El-Bakkari, J. El-Hamouchi, A. Sali, F. Ungan, Nonlinear optical properties of a single donor dopant in multilayered quantum dots under an electric field, Phys. B 716 (2025) 417701, http://dx.doi.org/10.1016/j.physb.2025.41770119.
[26] M. Jaouane, A. Ed-Dahmouny, H.M. Althib, A. Alkhaldi, R. Arraoui, A. Fakkahi, H. Azmi, A. Sali, Finite element study of exciton energies and optical absorption in InAs/GaAs multi-quantum dots under electric fields, Micro Nanostruct. 210 (2026) 208516, http://dx.doi.org/10.1016/j.micrna.2025.208516.
[27] D. Bejan, Impurity-related nonlinear optical rectification in double quantum dot under electric field, Phys. Lett. A 380 (2016) 3836–3842, http://dx.doi.org/10.1016/j.physleta.2016.09.020.
[28] D. Bejan, Effects of electric field and structure on the electromagnetically induced transparency in double quantum dot, Opt. Mater. 67 (2017) 145–154, http://dx.doi.org/10.1016/j.optmat.2017.03.031.
[29] A.H. Hameed, S. Hadi, F.K. Hachim, B.O. Al-Nashy, A.H. Al-Khursan, Optical bistability in double quantum dot structure, Chinese J. Phys. 94 (2025) 241–249, http://dx.doi.org/10.1016/j.cjph.2025.01.026.
[30] R. Ya. Leshko, H. Ya. Bandura, I.V. Bilynskyi, A.V. Karpyn, M.V. Kvyk, Ya. Yu. Melnyk, A.O. Ocheretyanyi, M. Yu. Popov, Effect of arbitrarily directed electric field on hole spectra and absorption in a quantum dot with off-center impurity, Phys. Lett. A 559 (2025) 130898, http://dx.doi.org/10.1016/j.physleta.2025.130898.

[31] N. Paul, S. Chattopadhyay, Design and modeling of resonant tunneling transport-controlled voltage-induced double quantum dot channel nanowire field-effect-transistor (DQD-FET) for multi-threshold current levels, Solid-State Electron. 230 (2025) 109259, http://dx.doi.org/10.1016/j.sse.2025.109259.
[32] F. Badshah, D.-Y. Lü, J. Xie, Z. Shi, Q. He, M. Idrees, Manipulation of photonic spin Hall effect via controllable double-tunneling induced transparency in quantum dot molecules, Opt. Laser Technol. 192 (2025) 113816, http://dx.doi.org/10.1016/j.optlastec.2025.113816.
[33] M.G. Barseghyan, V.N. Mughnetsyan, H.M. Baghramyan, F. Ungan, L.M. Pérez, D. Laroze, Control of electronic and optical properties of a laser dressed double quantum dot molecule by lateral electric field, Phys. E 126 (2021) 114362, http://dx.doi.org/10.1016/j.physe.2020.114362.
[34] M. Rontani, C. Cavazzoni, D. Bellucci, G. Goldoni, Full configuration interaction approach to the few-electron problem in artificial atoms, J. Chem. Phys. 124 (2006) 124102, http://dx.doi.org/10.1063/1.2179418.
[35] M. Ciurla, J. Adamowski, B. Szafran, S. Bednarek, Modeling of confinement potentials in quantum dots, Phys. E 15 (2002) 261–268, http://dx.doi.org/10.1016/S1386-9477(02)00572-6.